A Dual Layered Loop Array Antenna for Base Stations With Enhanced Cross-Polarization Discrimination

Can Ding, *Member, IEEE*, Hai-Han Sun, *Student Member, IEEE*, Richard W. Ziolkowski, *Fellow, IEEE*, and Y. Jay Guo, *Fellow, IEEE*

Abstract— This paper presents a novel dual-loop array antenna targeted at current and future base station applications. The antenna has four rectangular loops and four trapezoidal loops printed on the front and back sides, respectively, of a substrate placed above a flat square reflector. All eight loop radiators are excited simultaneously with properly designed feed networks to achieve its ±45° polarization states. The trapezoidal loops act like folded (electric) dipoles; the rectangular loops act primarily as magnetic dipoles. The combination of these two loop arrays leads to a type of magnetoelectric loop antenna that has stable directivity patterns with high cross-polarization discrimination (XPD) values across a 45.5% operational fractional bandwidth from 1.7 to 2.7 GHz. A fabricated and measured prototype confirms the simulation results and demonstrates that the half-power beamwidths in the horizontal plane vary between 63° and 70°, the XPD values are >20 dB in the boresight direction, and are >10 dB within the entire cellular coverage angular range: $-60° \le \theta \le 60°$.

Index Terms— Antenna array, base station antenna, cross-polarization discrimination (XPD), dual-polarization, loop antenna, magnetoelectric (ME) antenna, ME array.

I. INTRODUCTION

MODERN commercial base station antenna elements must meet several industry-recognized performance specifications. These specifications include good impedance matching to 50 Ω across a wide frequency range from 1.71 to 2.69 GHz, dual polarization, high port-to-port isolation, stable half-power beamwidth (HPBW), and high cross-polarization discrimination (XPD). There have been many antenna research activities in this area in recent years. Generally speaking, the reported antennas can be classified into three different types depending on their configurations and operating principles.

The first one employs crossdipoles, i.e., the radiating elements are a pair of dipoles that are oriented perpendicular
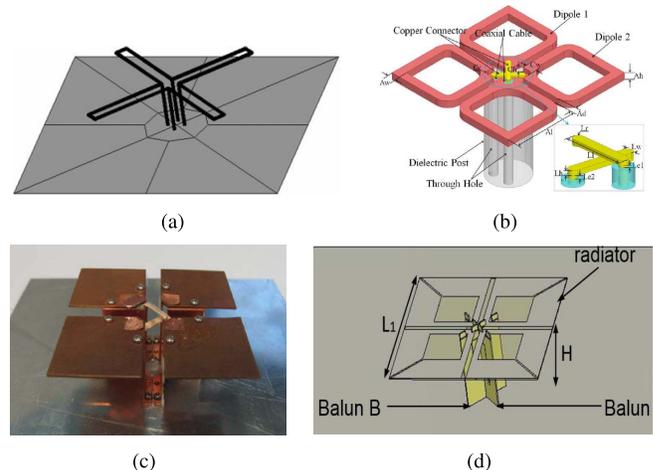
Fig. 1. Example configurations of different types of base station antennas. (a) Type-I "isolated" crossdipole [1]. (b) Type-I "tightly coupled" crossdipole [5]. (c) Type-II ME dipole [14]. (d) Type-III square array antenna [24].

to each other [1]–[12]. By exciting either one of the two subdipoles, different polarizations can be obtained. The basic crossdipole configurations used in early base station applications had the employed two dipoles "isolated" from each other, as shown in Fig. 1(a), resulting in bandwidths that were usually <25%. This limited bandwidth does not fully cover the 4G bands. More recently, it has been advocated to exploit crossdipoles with wider dipoles and to decrease the spacings between them, thus making them more tightly coupled to each other [3]–[12], as shown in Fig. 1(b). These configurations can have much wider bandwidths and improved the radiation performance. Nonetheless, their radiation patterns usually vary significantly with frequency. To achieve stable radiation patterns as required for the base station application, shaped reflectors are usually employed to compensate for the patterns changing with frequency. While these modified reflectors are acceptable in single band base station arrays, they may result in unwanted scattering to other antennas in advanced systems such as the current 4G dual-band array systems or the anticipated 5G massive MIMO systems [13].

The second type is based on magnetoelectric (ME) dipoles [14]–[19]. ME dipoles consist of a pair of crossed dipoles, a reflector, and a pair of patch antennas which are placed between the cross dipoles and the reflector [see Fig. 1(c)]. The advantage of the ME dipoles is the stability of their radiation

patterns across a wide band, a feature that arises from the complementary electric and magnetic currents generated on the dipole and patch radiators. Their effective electric and magnetic currents are orthogonal to each other, and they are all parallel to the ground plane. According to image theory [20], the corresponding radiation patterns vary in opposite ways with frequency, thereby generating stable combined patterns. The drawback of ME dipoles is the challenge to achieve an excellent impedance match, i.e., with VSWR < 1.5. Most of the published studies have moderate matching values, i.e., typically with VSWR < 2. A recently published ME dipole [19] has achieved excellent matching with VSWR < 1.5 and a high port-to-port isolation from 1.62 to 2.87 GHz. However, it appears that maintaining stable radiation patterns over this bandwidth with this structure is challenging.

The third type, referred to as a square array, utilizes four electric dipoles arranged in a square [13], [21]–[24] as shown in Fig. 1(d). By properly exciting them, dual slant-polarized, i.e., ±45° polarized, radiation can be achieved. This configuration type normally has a limited bandwidth, i.e., <25%. However, recently published papers [13], [24] have demonstrated a significantly enhanced impedance bandwidth, >45%, and the ability to maintain a stable radiation pattern over that frequency range.

It should be noted that most works have focused only on achieving excellent matching and stable HPBW. Even though a high XPD value has become another important criterion for base station antennas [25], [26], only a few systems have been reported which have achieved this goal. The XPD technical standards are >20 dB in the boresight direction and >10 dB within ±60° of the main lobe. While it is relatively easy to have the XPD > 20 dB at boresight, it is a real challenge to maintain the XPD > 10 dB over the entire coverage range, $-60° \leq \theta \leq 60°$.

Reference [25] first addressed the XPD issue, attaining good XPD values across a wide band. However, large parasitic elements were employed, which significantly enlarged the antenna aperture. Based on an equivalent model and a comprehensive quantitative analysis of dual slant-polarized antennas, it has been demonstrated that a large aperture is indeed required to enhance the XPD of a crossdipole configuration [12]. Nevertheless, in [26], vertical parasitic elements were placed between the crossdipole and its reflector to dramatically increase the XPD without increasing the aperture size. Unfortunately, the realized bandwidth was limited to 11.8%. Furthermore, it is noted that these XPD enhancing methods are all limited to crossdipole type configurations.

In this paper, a novel configuration that employs eight loop-based radiators that lead to stable radiation patterns and high XPD values across a very wide operational band is reported. In this antenna, a smaller loop array that employs four rectangular loop radiators is printed on the back side of a substrate and a larger loop array that is constructed with four trapezoidal loop radiators is printed on the front side. The antenna reported herein operates with a different mechanism when it is compared with the published ME dipoles that have one pair (single polarization) or two pairs (dual polarization) of electric current and magnetic current perpendicular to each
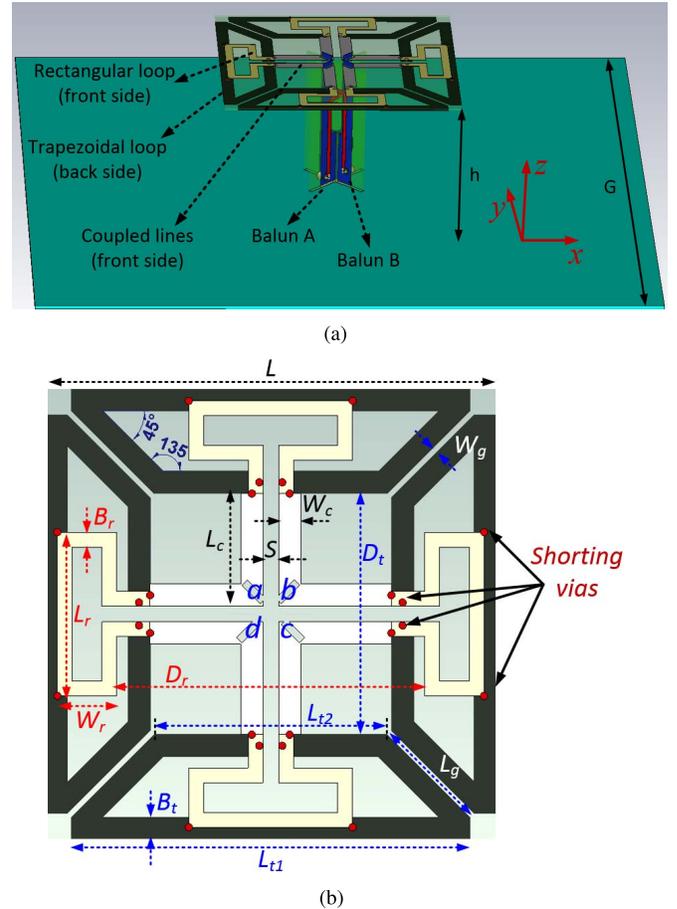

(a)

(b)

Fig. 2. Dual layered loop array antenna. (a) Detailed perspective view of the antenna. (b) Top view of the radiation aperture only.

other and parallel to the ground plane [14]–[18]. The eight radiating elements in the antenna reported support both magnetic and electric currents operating in concert, the magnetic ones being oriented in a direction perpendicular to the electric ones. The electric currents are parallel to the ground plane while the magnetic currents are normal to it. As a result, the fields radiated by the two loop arrays compensate for each other, leading to improved XPD values and stabilized HPBWs across a wide band. The experimental results demonstrate, in good agreement with their simulated values, that the XPD values are >20 dB at boresight and >10 dB within the coverage range, $-60° \leq \theta \leq 60°$. Impedance matching with $S_{11} < -10$ dB is achieved across a wide operational band, from 1.7 to 2.7 GHz, i.e., 1.0 GHz, yielding a fractional bandwidth (FBW) = 45.45% for base station applications. The attained HPBWs within this band are from 63° to 70°.

II. ANTENNA CONFIGURATION

Fig. 2(a) shows a detailed perspective view of the dual layered loop array antenna. It has an aperture consisting of eight loop radiators printed on the two sides of a substrate. Two baluns are employed to support these radiators and to achieve their ±45° polarization states. The antenna is placed on a flat square reflector whose size is $G \times G$. Fig. 2(b) illustrates the details of the radiating elements. A smaller loop

TABLE I

DESIGN DIMENSIONS (IN Millimeters)

Parameter	Value	Description
L	60.8	Aperture size
h	33	Antenna height
G	160	Reflector size
L_r	22	Length of rectangular loops
W_r	8	Width of rectangular loops
B_r	2	Strip width of rectangular loops
D_r	41.55	Distance between rectangular loops
L_{t1}	53.77	Edge length of trapezoidal loops 1
L_{t2}	31.5	Edge length of trapezoidal loops 2
L_g	15.75	Edge length of trapezoidal loops 3
W_g	0.74	Gap width between trapezoidal loops
D_t	32.55	Distance between trapezoidal loops
L_c	15.23	Length of coupled lines
W_c	3.0	Width of coupled lines
S	2.1	Distance between a pair of coupled lines

array consisting of four rectangular loops is printed on the front side of the substrate; a larger loop array consisting of four trapezoidal loops is printed on the back side. Four pairs of coupled lines used to excite the radiators are also printed on the front side of the substrate. Shorting vias are inserted into the substrate to connect the loop radiators printed on both of its sides and to facilitate them being excited coherently. These shorting vias also prevent unwanted resonances that might result from the coupling between the radiators in both the arrays. The substrate employed in this paper is a 0.5 mm thick piece of FR4. Its relative dielectric constant is 4.3, and its loss tangent is 0.021. The detailed dimensions of the radiators are given in Fig. 2(b) and their optimized values are given in Table I. The distance between this radiation aperture and the reflector is h. A more detailed description of the feed networks will be given in Section IV-B.

III. OPERATING PRINCIPLES

To better understand its working mechanisms, the antenna system was analyzed numerically. All of these simulations were conducted in CST Microwave Studio 2017. The analysis first focused on the eight loop radiators in the presence of the ground plane. They were excited simultaneously using four ideal discrete ports as shown in Fig. 3(a). The feed networks, including the coupled lines, were removed in these studies to improve the simulation time. These components were found to have only minor effects on the radiation pattern and were included later in the final optimization studies.

A. Current Distribution

The current distributions at the center frequency 2.2 GHz on the small and large loop arrays are illustrated in Fig. 3(b) and (c), respectively. Two current monitors (C1 and C2) were used to sample the current at indicated specific points, i.e., they were applied to the middles of the outer sides of the rectangular and trapezoidal loops as shown in Fig. 3(a). The monitored values are given in Fig. 4. They provided a means to calculate the magnitudes and phases of the currents on the radiators of both the loop arrays.

The currents induced on the rectangular loops are illustrated in Fig. 3(b). The stronger components of these currents
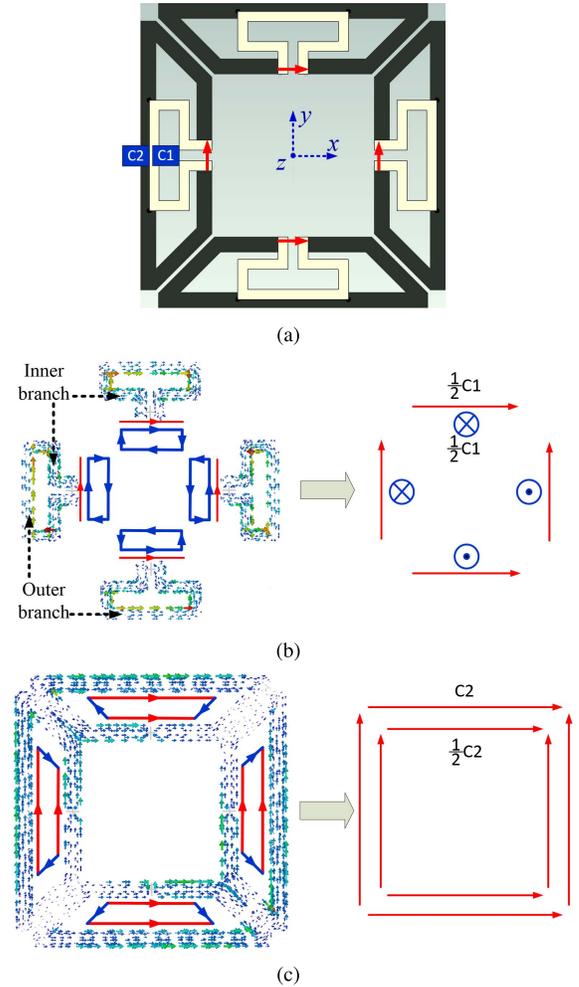

Fig. 3. Models of the radiating elements. (a) Simplified model with ideal excitations. Surface current distribution on the (b) front side of the small rectangular loops and (c) back side of the large trapezoidal loops at the center frequency, 2.2 GHz.

reside on their inner edges. The currents forming the magnetic dipoles are clearly identifiable. The orientation of each magnetic dipole, as depicted in the right subplot, follows immediately from the direction of the currents in the corresponding loop. The currents on the outer branches of the inner edges can be effectively decomposed into two pieces: a strong electric component and the magnetic component along it that completes the loop current. The electric dipoles are clearly oriented by the current directions along those outside branches, as depicted in the right subplot. As a result, each rectangular loop acts as the magnetic and electric dipole combinations illustrated in the right subplot. These features are also emphasized with the red and blue current direction inserts in the left subplot.

The currents on the trapezoidal loops are illustrated in Fig. 3(c). They have a standard folded dipole behavior [20]. They are concentrated on the inner and outer edges of the trapezoids as shown in the left subplot. Moreover, they can be generally considered to be in phase. As a consequence, these currents can be viewed simply as a combination of two linear electric currents as depicted in the right subplot.
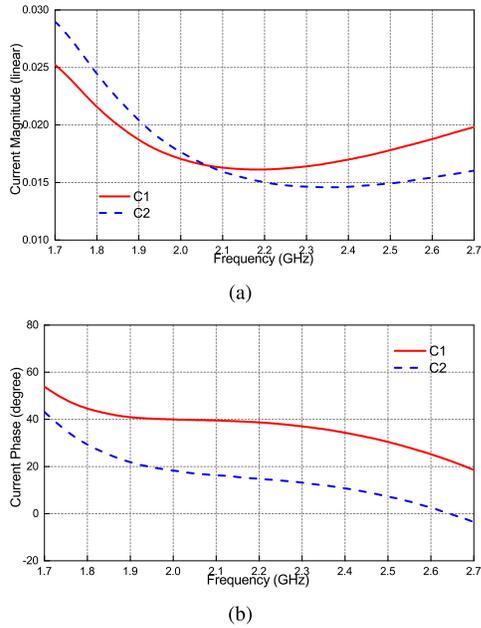
Fig. 4. (a) Magnitudes and (b) phases of the current monitors C1 and C2.

By applying more current monitors at different positions on the rectangular and trapezoidal loops, more accurate current density distribution information was attained. It was found that the weighting factors of the various current components can be approximated as $(1/2)C1 : (1/2)C1$ for the rectangular loops and as $C2 : (1/2)C2$ for the trapezoidal loops. These factors are explicitly shown in the right subplots of Fig. 3(b) and (c).

Fig. 4(a) and (b) shows the simulated magnitudes and phases of the currents measured by monitors C1 and C2, respectively. It was determined from these values that at the middle of the outer sides of the rectangles and trapezoids, where they reach their peak values, the currents have similar magnitudes, i.e., $|C1| \approx |C2|$, and small phase differences, i.e., $<20°$. This behavior is expected since the outer sides of the loops are shorted using vias. Note that the electric currents dominate the copolarization radiation patterns. The magnetic currents only help mitigate the cross-polarization radiation. Since the current densities of the electric current on the larger loops are much stronger ($1.5 \times |C2|$) than those on the smaller loops ($0.5 \times |C1|$), the characteristics of the fields radiated by the system are dominated by them.

B. Radiation Pattern

To explore the differences between exciting each array separately and both arrays simultaneously, we have plotted their copolarization and cross-polarization directivity patterns in Fig. 5(a)–(c), respectively. The simulations were conducted with the ground plane being present. Six frequency samples, $f = 1.7, 1.9, 2.1, 2.3, 2.5,$ and 2.7 GHz, were selected across the target band in each case. Moreover, note that the directivity patterns generated by the small and large loop arrays presented in Fig. 5(a) and (b), respectively, were obtained by exciting only one array and removing the other array from simulation.

It is observed from these results that the cross polarization level at $\theta = \pm 60°$ is noticeably lower when both arrays
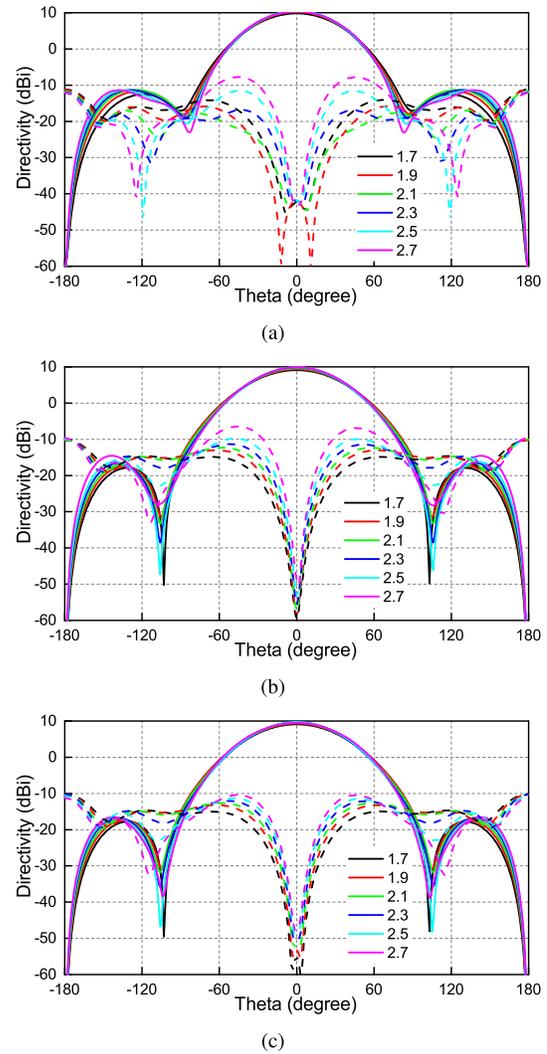

Fig. 5. Simulated copolarization and cross-polarization directivity patterns in the horizontal plane at the frequency points: 1.7, 1.9, 2.1, 2.3, 2.5, and 2.7 GHz. They are represented, respectively, by the solid and dashed lines. (a) Four small loops only. (b) Four large loops only. (c) All eight loops.

are excited together. This outcome was the main goal of this paper. Moreover, while the copolarization patterns shown in Fig. 5(b) and (c) are almost identical, they are different from those shown in Fig. 5(a). This behavior confirms that the larger loop array dominates the radiation performance in the horizontal plane and that the smaller one contributes only a little to the cross-polarization patterns.

To explicitly show the performance enhancement offered by the two loop array combinations, the HPBWs and XPDs of the three different cases shown in Fig. 5 are compared in Fig. 6. Note that the XPDs plotted here are the minimum values within the $-60° \leq \theta \leq +60°$ region in the horizontal plane. As shown in the figure, the XPD can be maintained >10 dB only when the two loop arrays are working together. The XPDs of the other two cases both decrease when the frequency $f \geq 2.1$ GHz. When only the large loop array is excited, the XPD is ≤ 10 dB across the band from 2.3 to 2.7 GHz, which occupies 40% of the entire operational band. When only the small loop array is excited, the results seem to be acceptable since the
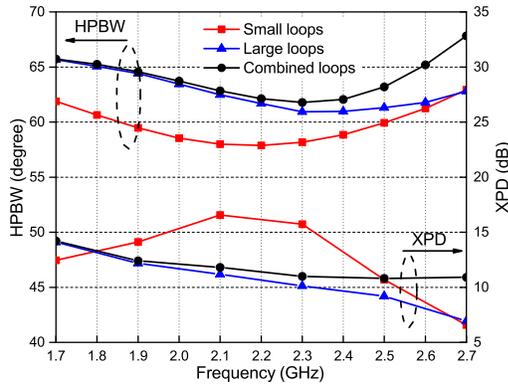
Fig. 6. Comparison of the simulated HPBW and the minimum XPD values within the angular range $-60° \leq \theta \leq +60°$ in the horizontal plane. They were obtained from the directivity patterns generated by the rectangular loop array only, the trapezoidal loop array only, and by both arrays together.
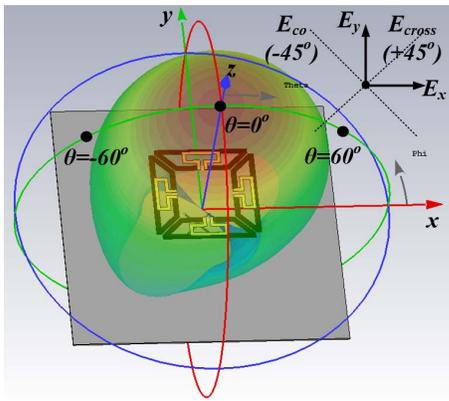

Fig. 7. Schematic 3-D directivity pattern of the optimized dual-loop array antenna.

XPD is ≤ 10 dB only in a small percentage of the operational band, i.e., in the interval $2.55 \leq f \leq 2.7$. Moreover, the XPD is quite high for the operational band. However, the HPBW is quite narrow, which is unwanted. Base station antennas usually are required to have stable HPBW values of $65° \pm 5°$ across their entire operation frequency band [12]. Furthermore, the antenna cannot be matched across the target band since the aperture is not large enough.

C. XPD Analysis

As suggested in [12], the XPD of this $\pm 45°$ polarized antenna in the horizontal, xz, plane was examined by decomposing the far field shown in Fig. 7 into its x- and y-polarized components

$$\widehat{x} \cdot \overrightarrow{E} = E_x e^{j\phi_x}, \quad \widehat{y} \cdot \overrightarrow{E} = E_y e^{j\phi_y}. \tag{1}$$

Then, the copolarized and cross-polarized field vectors can be expressed as follows:

$$E_{co} = \cos\frac{\pi}{4} E_x e^{j\phi_x} + \cos\frac{\pi}{4} E_y e^{j\phi_y}$$
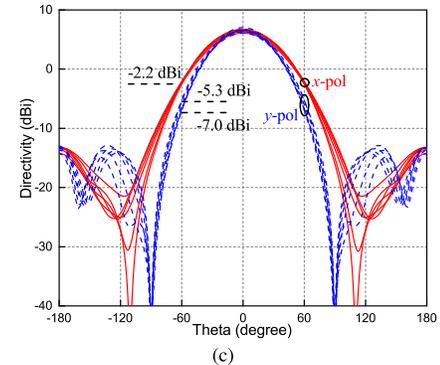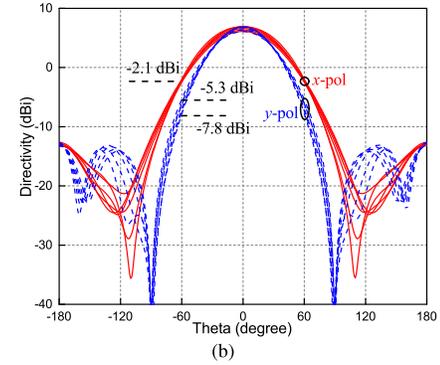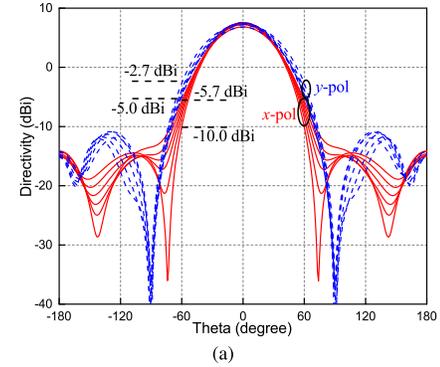$$E_{cross} = \cos\frac{\pi}{4} E_x e^{j\phi_x} - \cos\frac{\pi}{4} E_y e^{j\phi_y}. \tag{2}$$

Fig. 8. Simulated x- and y-polarized directivity patterns in the horizontal plane at the frequency points: 1.7, 1.9, 2.1, 2.3, 2.5, and 2.7 GHz. They are represented by the solid and dashed lines, respectively. (a) Rectangular loop array. (b) Trapezoidal loop array. (c) Dual-loop array.

The XPD is the ratio of the magnitudes of these copolarized and cross-polarized vectors

$$\text{XPD} = \left| \frac{E_{co}}{E_{cross}} \right| = \sqrt{\frac{E_x^2 + E_y^2 + 2E_x E_y \cos(\phi_x - \phi_y)}{E_x^2 + E_y^2 - 2E_x E_y \cos(\phi_x - \phi_y)}}. \tag{3}$$

It is assumed that $\phi_x = \phi_y$ in [12] to simplify the analysis, since both the E_x and E_y components arrive at approximately the same time when one observes the field at a point infinitely far away. Then, (3) can be rewritten as

$$\text{XPD} = \sqrt{\frac{E_x^2 + E_y^2 + 2E_x E_y}{E_x^2 + E_y^2 - 2E_x E_y}} = \left| \frac{E_x + E_y}{E_x - E_y} \right|. \tag{4}$$

It is thus concluded that a high XPD is achieved if the difference between the magnitudes of the radiated x- and y-polarized field components, $|E_x|$ and $|E_y|$, is as small as possible.

To have a deeper understanding of how the high XPD value is attained, Fig. 8 shows the comparison of the
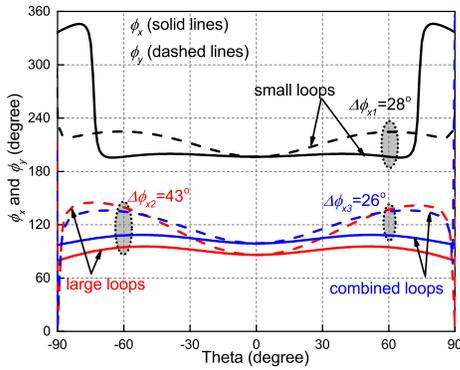
Fig. 9. Simulated phases of the x- and y-polarized radiated fields in the horizontal plane at 2.7 GHz for the rectangular loop array only, the trapezoidal loop array only, and the dual-loop array. These values are represented by the solid and dashed lines, respectively.

x- and y-polarized directivity patterns generated by the rectangular loop array, by the trapezoidal loop array, and by both two arrays together. Notice that the discrepancy between the E_x and E_y values is very small at $\theta = 0°$ but gets much larger as observation direction approaches $\theta = \pm 60°$ for all the three cases. This explains why the XPD values at the edges of the target angular region in the horizontal plane are much smaller than those at boresight. In particular, as shown in Fig. 8(a), the x-polarized patterns are narrower than the y-polarized ones when only the smaller rectangular loop array is excited. Although it is difficult to discern in the figure, the x- and y-polarized patterns are getting narrower and wider, respectively, as the frequency increases. To be specific, at $\theta = \pm 60°$, the discrepancy between the E_x and E_y component values increases from $E_x/E_y = -5.7$ dBi + 5.0 dBi = -0.7 dB to $E_x/E_y = -10.0$ dBi +2.7 dBi = -7.3 dB as the frequency increases from 1.7 to 2.7 GHz.

In contrast, Fig. 8(b) demonstrates that the x-polarized patterns are wider than the y-polarized ones when only the larger trapezoidal array is excited. Moreover, the x-polarized patterns are quite stable and the y-polarized patterns are becoming narrower as the frequency increases. Consequently, the XPD, in this case, is also getting smaller in agreement with the results shown in Fig. 5(b).

As shown in Fig. 8(c), the x- and y-polarized directivity patterns radiated by the loop array combination are quite similar to those of a single trapezoidal loop array. Although E_x/E_y shown in Fig. 8(c) is slightly smaller than that in Fig. 8(b), the reduction is not significant enough to produce a large XPD enhancement according to (4). It reduces 5 dB at 2.7 GHz as shown in Fig. 6. Consequently, there must still be another factor that contributes to the XPD enhancement.

We found in our studies that while the addition of the smaller rectangular loop array to the larger trapezoidal loop array only slightly changes the magnitudes of the E_x and E_y components, it impacts their phases. Therefore, it was determined that it is inappropriate to assume their phases are equal, i.e., $\phi_x = \phi_y$. Fig. 9 plots ϕ_x and ϕ_y using solid and dashed lines, respectively, for the three different array cases at 2.7 GHz. The simulated phase values are illustrated in black, red, and blue color when, respectively, only the

smaller rectangular loop array, only the larger trapezoidal loop array, or both loop arrays are excited. Notice that the phase differences: $\Delta\phi = |\phi_x - \phi_y|$, for all the three cases are near zero at $\theta = 0°$ and increase with $|\theta|$. According to (3), it can then be deducted that the smaller $\Delta\phi$, the higher the XPD value. Therefore, although the directivity pattern is observed to be dominated by the larger trapezoidal loop array contributions, the presence of the smaller rectangular loop array reduces the phase difference from $\Delta\phi_2 = 43°$ to $\Delta\phi_3 = 26°$ at $\theta = \pm 60°$, thereby leading to the observed higher XPD values when the dual-loop array is excited.

IV. ANTENNA DESIGN

A. Parametric Study

The previous analysis demonstrated why high XPD values are realized across a wide band when both the loop arrays are operating in concert. Further investigations were necessary to learn how to adjust the design dimensions to optimize its performance characteristics. Therefore, more parameter sweeps were conducted. Because the dual-loop array antenna configuration has many adjustable parameters, only three representative dimensions, L_{t2}, L_r, and D_t, will be discussed. By changing them, the size of the trapezoidal loops, the size of the rectangular loops, and the distance between the trapezoidal loops (and hence the size of the aperture) are changed, respectively. The performance factors concerned in these studies were the XPD, HPBW, and the input impedance. Because the feed networks are not yet included, the input impedance values are determined at the excitation ports, as shown in Fig. 3(a).

In particular, when L_{t2} was varied, all of the other parameters were fixed except for L_{t1}. This sweep was performed with the base angles of the trapezoid being maintained and, hence, L_{t1} also had to be varied. Similar adjustments had to occur with the other parameter variations. For instance, adjusting D_t, the separation distance between the trapezoidal array elements, D_r had to be varied appropriately to maintain the relative positions and sizes of the rectangular loops. Note that the size of the entire aperture changes when D_t is varied, and the area of the rectangular loops change when L_r is varied. The effects of these parameter variations on the directivity patterns and the input impedance are illustrated in Fig. 10.

As observed in Fig. 10(a), changing the size of the rectangular loops almost has no effect on the HPBW and XPD values. This outcome is mainly due to the fact that the directivity patterns are dominated by the currents on the larger trapezoidal loops. Fig. 10(b) demonstrates that the effect of the trapezoidal loop size on the radiation performance is also not significant. This outcome illustrates the robustness of this configuration. On the other hand, Fig. 10(a) and (b) shows that changes in the sizes of the two different loop types lead to noticeably different input impedance values. These results lead to the conclusion that the length of the loops can be used effectively to tune the impedance without having to worry about a significant change in the radiation performance.

Furthermore, as Fig. 10(c) indicates, the radiation performance is sensitive to the separation distance D_t between the
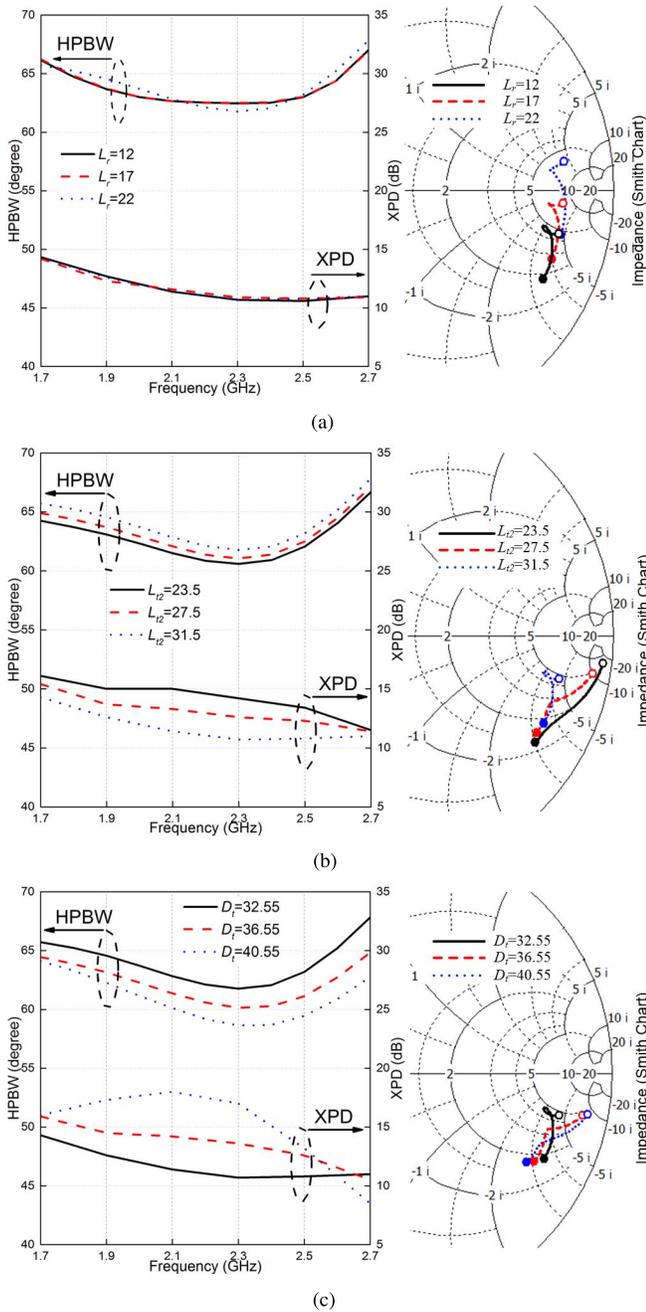
Fig. 10. Parameter sweep results given as a plot of the HPBW and XPD values in the horizontal plane as functions of the source frequency and as a Smith chart plot of the input impedance values. (a) L_r, rectangular loop size. (b) L_{t2}, trapezoidal loop size. (c) D_t, the distance between the loop radiators.

array elements. This is expected because the aperture size is a key factor in the shape of the directivity pattern. Meanwhile, D_t also has some effects on the input impedance. It impacts the mutual coupling levels between the adjacent loops. In addition, the antenna height h and the ground plane size G are also key factors in determining the directivity pattern and, hence, in optimizing the HPBW and XPD values. However, they have only a minor effect on the input impedance. Because they have been studied and reported previously [12], details of the effects on the performance of base station antennas caused by variations in the design parameters h and G will not be repeated here.
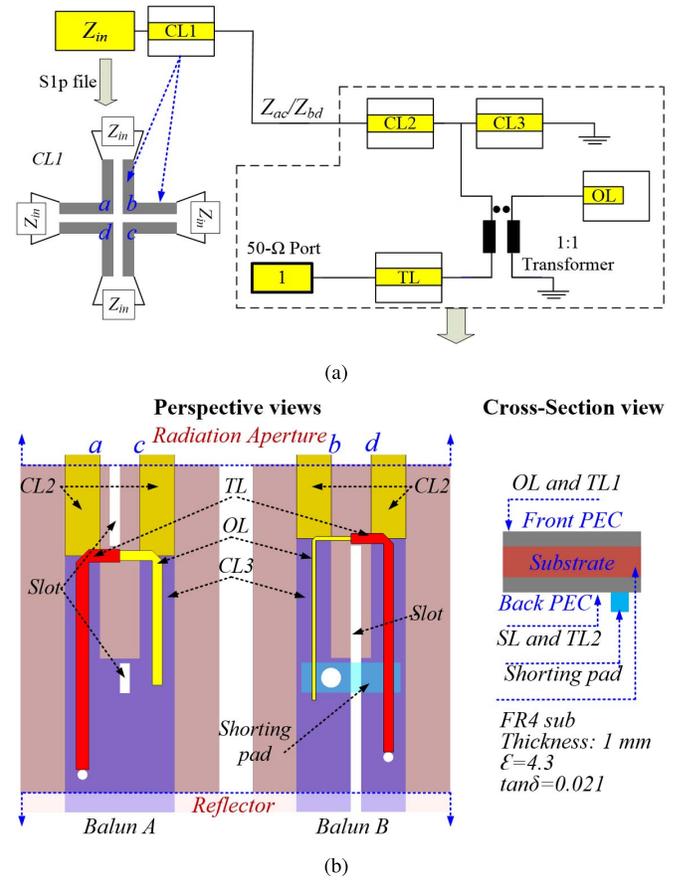

Fig. 11. Feed networks. (a) Circuit theory model. (b) Physical implementation.

B. Impedance Matching

It was found that to optimize dual-loop antenna performance, it was best to first consider the antenna height h, the reflector size G, and the antenna aperture size. The length and width of the loops were then be adjusted to achieve a satisfactory input impedance match across the target frequency band. To design the feed network, the input impedances, Z_{in}, at the excitation ports shown in Fig. 3(a) were exported from the full-wave simulator as S1p files and imported into the matching circuit model shown in Fig. 11(a). By optimizing this matching circuit with circuit simulations, which are faster and more cost-effective than those in a full-wave simulator, it was determined that the antenna could be matched to the source. Once the optimized circuit parameters were attained, a 3-D model of the feed network was then built and adjusted with full-wave simulations. The final design is shown in Fig. 11(b). The matching circuit consists of two major parts. The first part is four pairs of coupled lines (CL1) printed on the same surface as the loop radiators. As shown in Figs. 11(a) and 2(a), the traces CL1 link all of the loop radiators together. Therefore, by placing a differential voltage across ac or bd, all of the loop radiators can be excited to achieve the desired $\pm45°$ dual polarization.

This filter type of impedance matching feed network was first proposed in [27] and then used in [12] and [13] for base station antennas. The principle is to utilize several segments

TABLE II
DIMENSIONS OF THE TWO FEED NETWORKS (IN MILLIMETERS)

--	Feed network A			Feed network B		
(mm)	Length	Width	Distance	Length	Width	Distance
CL1	15.22	3.0	2.16	15.22	3.0	2.16
CL2	8.5	3.5	4.0	8.5	3.5	4.0
CL3	10.32	3.5	4.0	12.02	3.5	4.0
TL	23.95	1.3	--	24.25	1.0	--
OL	15.75	1.0	--	19.65	0.4	--

of transmission lines (TLs) together with the impedance of the antenna itself to construct both a bandpass filter and a resistance transformer to mitigate, respectively, the variations of the reactance and the resistance of the input impedance. The matching components and their arrangement are not fixed. They can be adjusted subject to the geometrical constraints placed on the system.

The other part of the feed network illustrated in Fig. 11(b) is a set of baluns. They are oriented perpendicular to the radiation aperture and the reflector. This arrangement transfers Z_{ac}/Z_{bd} into 50 Ω. It provides geometrical support to the radiators. These baluns are composed of four components: two pairs of coupled lines, CL2 and CL3; an open circuit line (OL); and a TL. As shown in Fig. 11(b), CL2 and CL3 are printed on the back side of the substrate and are shorted to the ground (reflector). They work as the back (ground plane) metal for the microstrip lines TL and OL that are printed on the front side of the substrate. The 1:1 transformer shown in Fig. 11(a) represents the coupling between these microstrip lines and the coupled lines printed on the front and back sides of the substrate, respectively.

Slots are etched into the two feed networks for assemblage. To avoid overlap, these two feed networks are designed to be slightly different. In particular, the length of CL2 in each has a different value. This feature subsequently leads to different dimension values for the components CL3, OL, and TL for the two feed networks to retune the impedance back to 50 Ω. Table II gives the dimensions of these two feed network designs. Note that the TL and OL are all bent toward the middle. Their lengths in Table II are the total lengths of the two segments.

V. RESULTS

The optimized dual-loop antenna was fabricated and measured. Fig. 12 shows a photograph of the fabricated prototype. Note that one can see the trapezoidal loops printed on the back side because the substrate is semi-transparent. The S-parameters of this antenna were measured in the RF lab of the Global Big Data Technologies Centre (GBDTC), University of Technology Sydney, Sydney, Australia. Fig. 13(a) and (b) shows the simulated and measured reflection coefficients and transmission coefficients of the two ports, respectively. It is observed that the measured results agree quite well with their simulated values. Across the target band from 1.7 to 2.7 GHz, the magnitudes of the measured reflection coefficients of the two ports, $|S_{11}|$ and $|S_{22}|$, are < -10 dB and those of the measured transmission coefficients, $|S_{12}|$ and $|S_{21}|$, are < -23 dB. Thus, the antenna
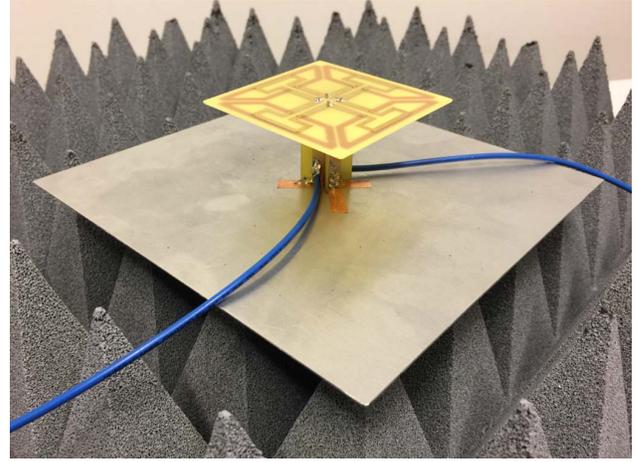

Fig. 12. Photograph of the fabricated antenna prototype.
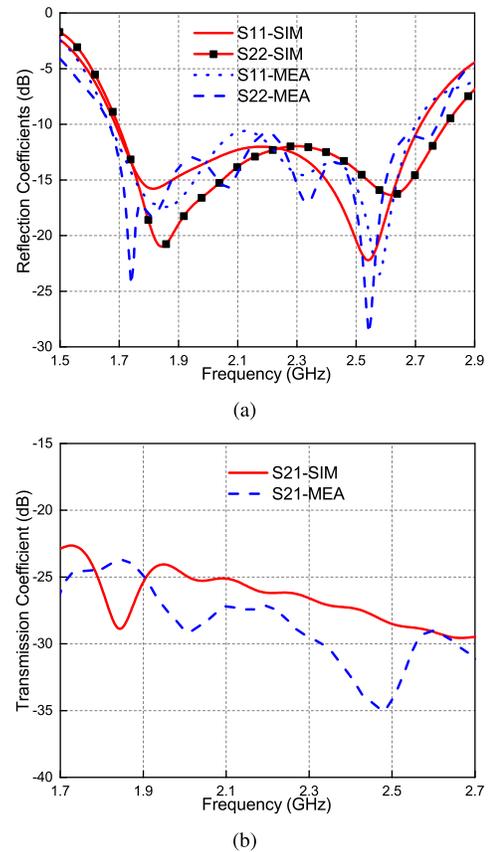

(a)

(b)

Fig. 13. Simulated and measured S-parameters of the dual-loop array antenna prototype. (a) Reflection coefficients. (b) Transmission coefficients.

has a 1.0 GHz bandwidth and, hence, an FBW = 45.5%. Note that only the $|S_{21}|$ results are given in Fig. 13(b) since the $|S_{12}|$ results are essentially the same.

The radiation performance of the dual-loop antenna prototype was measured at the outdoor antenna range owned by Vecta Pty Ltd [28], located in Castle Hill, Sydney, Australia. The measured and simulated copolarization and cross-polarization directivity patterns in the horizontal plane are shown in the Cartesian form in Fig. 14. Four frequency samples were selected within the operational band, 1.7 to 2.7 GHz.
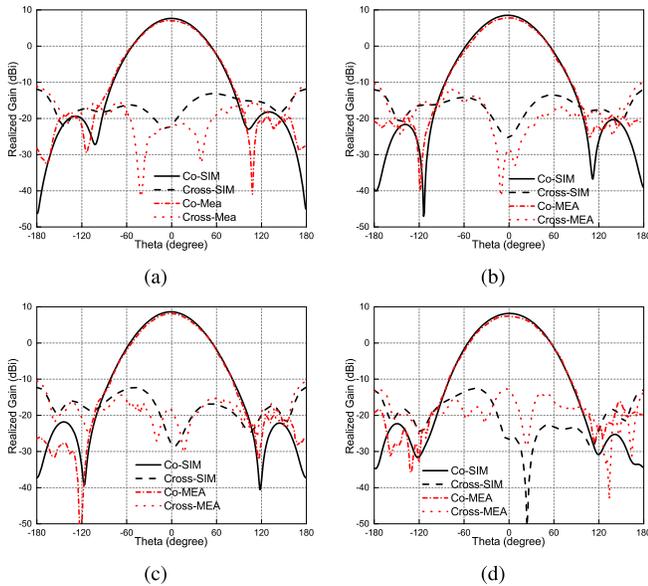
Fig. 14. Simulated and measured copolarization and cross-polarization directivity patterns of the dual-loop antenna prototype in its horizontal plane at (a) 1.7, (b) 2.0, (c) 2.4, and (d) 2.7 GHz.
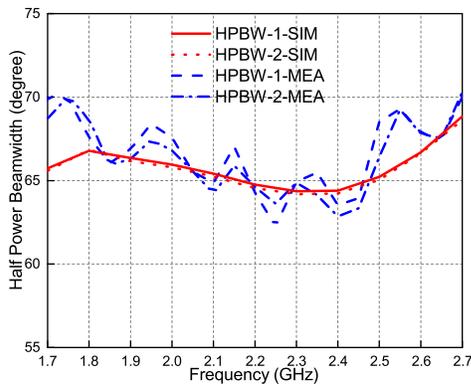

Fig. 15. Simulated and measured HPBWs of the dual-loop antenna prototype in its horizontal plane.
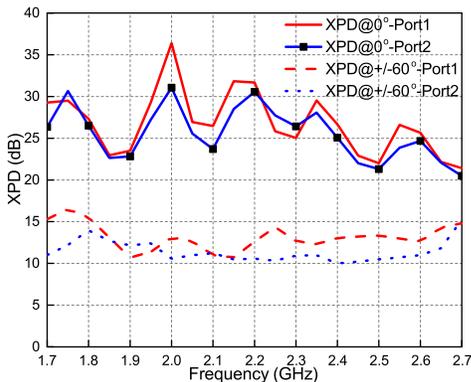

Fig. 16. Measured XPD values of the dual-loop antenna prototype at boresight, $\theta = 0°$, and at the edges of its angular coverage, $\theta = \pm60°$.

As illustrated in the figure, nearly identical patterns were achieved across the band; and the measured results agree very well with the simulated ones. Fig. 15 gives the simulated and measured HPBWs in the horizontal plane of the dual-polarization directivity patterns. It confirms that the stable

radiation patterns were attained, their HPBWs varying from 63° to 70° for both the polarizations. The measured XPD results are illustrated in Fig. 16. It can be seen that the measured XPDs are >20 dB at boresight and are >10 dB within the entire $-60° \leq \theta \leq 60°$ angular range.

VI. CONCLUSION

A novel dual-loop array antenna for base station applications was reported that has a wide band and is dual polarized with enhanced XPD values. The design consists of two loop arrays, one with four rectangular loops and one with four trapezoidal loops, printed on two sides of a substrate. The larger trapezoidal loops behave like folded dipoles having an electric current character. The smaller rectangular loops support loop currents and, hence, act primarily as loop radiators acting as magnetic dipoles. Comparisons were made between the radiation performance attained by exciting only the smaller rectangular array and only the larger trapezoidal loop array, as well as the two array combination to demonstrate the superior performance characteristics of the dual-loop array configuration. Current distributions on the radiators were presented along with a theoretical analysis to explain the origin of its enhanced XPD values. Parameter studies were discussed to show the robustness of this configuration. The antenna's feed networks were shown to be designed to excite the two arrays simultaneously with good impedance matching.

A prototype dual-loop antenna was fabricated and tested. The measured results, in good agreement with their simulated values, demonstrate that across its operational band from 1.7 to 2.7 GHz (100 MHz BW and FBW = 45.5%), the S_{11} and S_{22} values of its two ports are <-10 dB, and its S_{12} and S_{21} values are <-23 dB. The measured HPBWs are $66.5° \pm 3.5°$, the XPD values at $\theta = 0°$ are >20 dB, and the minimum XPD values within the $-60° \leq \theta \leq 60°$ angular range are >10 dB. The attained XPD values, impedance match, isolation, and stable radiation patterns make the reported dual-loop array antenna attractive for base station applications. Moreover, the approach of adding additional magnetic radiators to improve the XPD values established herein could also be applied to other dual-polarized antenna designs.

REFERENCES

[1] H. D. Hristov, H. Carrasco, R. Feick, and B. L. Ooi, "Low-profile X antenna with flat reflector for polarization diversity applications," *Microw. Opt. Technol. Lett.*, vol. 51, no. 6, pp. 1508–1512, 2009.
[2] H. D. Hristov, H. Carrasco, R. Feick, and G. S. Kirov, "Broadband two-port X antenna array with flat reflector for polarization diversity applications," *Microw. Opt. Technol. Lett.*, vol. 52, no. 12, pp. 2833–2837, Dec. 2010.
[3] Y. Liu, H. Yi, F.-W. Wang, and S.-X. Gong, "A novel miniaturized broadband dual-polarized dipole antenna for base station," *IEEE Antennas Wireless Propag. Lett.*, vol. 12, pp. 1335–1338, 2013.
[4] Y. Gou, S. Yang, J. Li, and Z. Nie, "A compact dual-polarized printed dipole antenna with high isolation for wideband base station applications," *IEEE Trans. Antennas Propag.*, vol. 62, no. 8, pp. 4392–4395, Aug. 2014.
[5] Z. Bao, Z. Nie, and X. Zong, "A novel broadband dual-polarization antenna utilizing strong mutual coupling," *IEEE Trans. Antennas Propag.*, vol. 62, no. 1, pp. 450–454, Jan. 2014.

[6] Y. Cui, R. Li, and H. Fu, "A broadband dual-polarized planar antenna for 2G/3G/LTE base stations," *IEEE Trans. Antennas Propag.*, vol. 62, no. 9, pp. 4836–4840, Sep. 2014.

[7] Q. X. Chu, D. L. Wen, and Y. Luo, "A broadband ±45° dual-polarized antenna with Y-shaped feeding lines," *IEEE Trans. Antennas Propag.*, vol. 63, no. 2, pp. 483–490, Feb. 2015.

[8] S. X. Ta, I. Park, and R. W. Ziolkowski, "Crossed dipole antennas: A review," *IEEE Antennas Propag. Mag.*, vol. 57, no. 5, pp. 107–122, Oct. 2015.

[9] B. B. Jones and J. K. A. Allan, "Ultra-wideband dual-band cellular base station antenna," U.S. Patent 0 139 387 A1, May 22, 2014.

[10] H. Huang, Y. Liu, and S. Gong, "A broadband dual-polarized base station antenna with anti-interference capability," *IEEE Antennas Propag. Lett.*, vol. 16, pp. 613–616, 2017.

[11] D.-Z. Zheng and Q.-X. Chu, "A multimode wideband ±45° dual-polarized antenna with embedded loops," *IEEE Antennas Propag. Lett.*, vol. 16, pp. 633–636, 2017.

[12] C. Ding, H. Sun, R. W. Ziolkowski, and Y. J. Guo, "Simplified tightly-coupled cross-dipole arrangement for base station applications," *IEEE Access*, vol. 5, pp. 27491–27503, 2017.

[13] H. Sun, C. Ding, B. Jones, and Y. J. Guo, "A wideband base station antenna element with stable radiation pattern and reduced beam squint," *IEEE Access*, vol. 5, pp. 23022–23031, 2017.

[14] B. Q. Wu and K. M. Luk, "A broadband dual-polarized magneto-electric dipole antenna with simple feeds," *IEEE Antennas Wireless Propag. Lett.*, vol. 8, pp. 60–63, 2009.

[15] K.-M. Luk and B. Wu, "The magnetoelectric dipole—A wideband antenna for base stations in mobile communications," *Proc. IEEE*, vol. 100, no. 7, pp. 2297–2307, Jul. 2012.

[16] H. Zhai, J. Zhang, Y. Zang, Q. Gao, and C. Liang, "An LTE base-station magnetoelectric dipole antenna with anti-interference characteristics and its MIMO system application," *IEEE Antennas Wireless Propag. Lett.*, vol. 14, pp. 906–909, 2015.

[17] G. Idayachandran and R. Nakkeeran, "Compact magneto-electric dipole antenna for LTE femtocell base stations," *Electron. Lett.*, vol. 52, no. 8, pp. 574–576, Apr. 2016.

[18] L. Mingjian, K.-M. Luk, K. Zhang, and L. Ge, "Miniaturization of magnetoelectric dipole antenna by using metamaterial loading," *IEEE Trans. Antennas Propag.*, vol. 64, no. 11, pp. 4914–4918, Nov. 2016.

[19] S.-G. Zhou, Z.-H. Peng, G.-L. Huang, and C.-Y.-D. Sim, "Design of a novel wideband and dual-polarized magnetoelectric dipole antenna," *IEEE Trans. Antennas Propag.*, vol. 65, no. 5, pp. 2645–2649, May 2017.

[20] C. D. Balanis, *Antenna Theory: Analysis and Design*, 4th ed. New York, NY, USA: Wiley, 2015.

[21] Y. H. Huang, Q. Wu, and Q. Z. Liu, "Broadband dual-polarised antenna with high isolation for wireless communication," *Electron. Lett.*, vol. 45, no. 14, pp. 714–715, Jul. 2009.

[22] S.-G. Zhou, P.-K. Tan, and T.-H. Chio, "Low-profile, wideband dual-polarized antenna with high isolation and low cross polarization," *IEEE Antennas Wireless Propag. Lett.*, vol. 11, pp. 1032–1035, 2012.

[23] H. Huang, Y. Liu, and S. Gong, "A novel dual-broadband and dual-polarized antenna for 2G/3G/LTE base stations," *IEEE Trans. Antennas Propag.*, vol. 64, no. 9, pp. 4113–4118, Sep. 2016.

[24] H. Sun, C. Ding, T. S. Bird, and Y. J. Guo, "A base station antenna element with simple structure but excellent performance," in *Proc. 3rd Austral. Microw. Symp.*, Brisbane, QLD, Australia, Feb. 2018, pp. 35–36.

[25] Y. Luo, Q.-X. Chu, and D.-L. Wen, "A plus/minus 45 degree dual-polarized base-station antenna with enhanced cross-polarization discrimination via addition of four parasitic elements placed in a square contour," *IEEE Trans. Antennas Propag.*, vol. 64, no. 4, pp. 1514–1519, Apr. 2016.

[26] Y. Luo, Q.-X. Chu, and J. Bornemann, "Enhancing cross-polarisation discrimination or axial ratio beamwidth of diagonally dual or circularly polarised base station antennas by using vertical parasitic elements," *IET Microw., Antennas Propag.*, vol. 11, no. 9, pp. 1190–1196, Jul. 2017.

[27] C. Ding, B. Jones, Y. J. Guo, and P.-Y. Qin, "Wideband matching of full-wavelength dipole with reflector for base station," *IEEE Trans. Antennas Propag.*, vol. 65, no. 10, pp. 5571–5576, Oct. 2017.

[28] *VectaLabs*. Accessed: Oct. 25, 2017. [Online]. Available: http://vectalabs.com
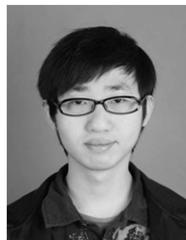
Can Ding (M'16) received the bachelor's degree in micro-electronics from Xidian University, Xi'an, China, in 2009, and the Ph.D. degree from Macquarie University, Sydney, Australia, in 2015.

From 2012 to 2015, he was with Macquarie University and Xidian University under the Cotutelle agreement. From 2015 to 2017, he was a Post-Doctoral Research Fellow with the University of Technology Sydney (UTS), Sydney. He is currently a Lecturer with Global Big Data Technologies Centre, UTS. He is with Commonwealth Scientific and Industrial Research Organisation DPaS Flagship, Marsfield, Australia. His current research interests include reconfigurable antenna, phase shifter, base station antenna, and terahertz waveguides.
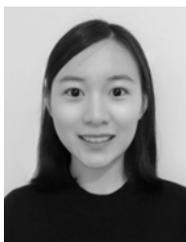
Hai-Han Sun (S'17) was born in Binzhou, Shandong, China, in 1994. She received the bachelor's degree in electronic information engineering from the Beijing University of Posts and Telecommunications, Beijing, China, in 2015. She is currently pursuing the Ph.D. degree in engineering with the University of Technology Sydney, Sydney, Australia.

Her current research interests include base station antennas and wideband omnidirectional antennas.

Richard W. Ziolkowski (F'94) received the B.Sc. degree *(magna cum laude)* in physics from Brown University, Providence, RI, USA, in 1974, the M.S. and Ph.D. degrees in physics from the University of Illinois at Urbana–Champaign, Urbana, IL, USA, in 1975 and 1980, respectively, and the Honorary Doctor Technish Honoris Causa degree from the Technical University of Denmark, Kongens Lyngby, Denmark, in 2012.

He was the Computational Electronics and Electromagnetics Thrust Area Leader with the Lawrence Livermore National Laboratory, Engineering Research Division, Livermore, CA, USA, in 1990. He is currently a Distinguished Professor with the University of Technology Sydney, Global Big Data Technologies Centre, Ultimo, NSW, Australia. He is also a Litton Industries John M. Leonis Distinguished Professor with the Department of Electrical and Computer Engineering and a Professor with the College of Optical Sciences, The University of Arizona, Tucson, AZ, USA. He was a 2014 Thomas-Reuters Highly Cited Researcher. His current research interests include the application of new mathematical and numerical methods to linear and nonlinear problems dealing with the interaction of electromagnetic and acoustic waves with complex linear and nonlinear media, as well as metamaterials, metamaterial-inspired structures, and applications-specific configurations.

Dr. Ziolkowski is a Fellow of the Optical Society of America (OSA) in 2006, and the American Physical Society in 2016. He was the Australian DSTO Fulbright Distinguished Chair in *Advanced Science and Technology* from 2014 to 2015. He served as the President for the IEEE Antennas and Propagation Society in 2005. He is also actively involved with the URSI, OSA, and SPIE professional societies.

Y. Jay Guo (F'14) received the bachelor's and master's degrees from Xidian University, Xi'an, China, in 1982 and 1984, respectively, and the Ph.D. degree from Xian Jiaotong University, Xi'an, in 1987.

He is currently a Distinguished Professor and the Founding Director of Global Big Data Technologies Centre, University of Technology Sydney, Sydney, Australia. He served as the Director for Commonwealth Scientific and Industrial Research Organisation, Marsfield, Australia, in 2014, where he directing a number of ICT research portfolios. He held various senior leadership positions at Fujitsu, London, U.K., Siemens, London, and NEC, London. He has authored or co-authored over 400 research papers. He holds 22 patents in antennas and wireless systems. His current research interests include antennas, millimeter-wave and terahertz communications, and sensing systems as well as big data.

Dr. Guo is a Fellow of the Australian Academy of Engineering and Technology and the IET and a member of the College of Experts of Australian Research Council. He has chaired numerous international conferences. He was the International Advisory Committee Chair of the IEEE VTC2017, the General Chair of ISAP2015, iWAT2014, and WPMC'2014, and the TPC Chair of 2010 IEEE WCNC, and 2012 and 2007 IEEE ISCIT. He was a recipient of most prestigious Australian National Awards, and was named one of the most influential engineers in Australia in 2014 and 2015. He served as a Guest Editor for Special Issues on antennas for satellite communications and antennas and propagation aspects of 60–90 GHz wireless communications, both in IEEE TRANSACTIONS ON ANTENNAS AND PROPAGATION, Special Issue on communications challenges and dynamics for unmanned autonomous vehicles, the IEEE JOURNAL ON SELECTED AREAS IN COMMUNICATIONS, and Special Issue on 5G for mission critical machine communications, *IEEE Network Magazine*.